◆EXPERIMENTAL INVESTIGATION ◆

Aortic Hemodynamics After Thoracic Endovascular Aortic Repair, With Particular Attention to the Bird-Beak Configuration

Guido H. W. van Bogerijen, MD[1,2]; Ferdinando Auricchio, PhD[3,4]; Michele Conti, PhD[3]; Adrien Lefieux[4]; Alessandro Reali, PhD[3]; Alessandro Veneziani, PhD[5]; Jip L. Tolenaar, MD, PhD[1,2]; Frans L. Moll, MD, PhD[2]; Vincenzo Rampoldi, MD[1]; and Santi Trimarchi, MD, PhD[1]

[1]Policlinico San Donato IRCCS, Thoracic Aortic Research Center, University of Milan, Italy. [2]Department of Vascular Surgery, University Medical Center Utrecht, The Netherlands. [3]Department of Civil Engineering and Architecture, University of Pavia, Italy. [4]Center for Advanced Numerical Simulations, Istituto Universitario di Studi Superiori di Pavia, Italy. [5]Department of Mathematics and Computer Science, Emory University, Atlanta, Georgia, USA.

Purpose: To quantitatively evaluate the impact of thoracic endovascular aortic repair (TEVAR) on aortic hemodynamics, focusing on the implications of a bird-beak configuration.

Methods: Pre- and postoperative CTA images from a patient treated with TEVAR for post-dissecting thoracic aortic aneurysm were used to evaluate the anatomical changes induced by the stent-graft and to generate the computational network essential for computational fluid dynamics (CFD) analysis. These analyses focused on the bird-beak configuration, flow distribution into the supra-aortic branches, and narrowing of the distal descending thoracic aorta. Three different CFD analyses (A: preoperative lumen, B: postoperative lumen, and C: postoperative lumen computed without stenosis) were compared at 3 time points during the cardiac cycle (maximum acceleration of blood flow, systolic peak, and maximum deceleration of blood flow).

Results: Postoperatively, disturbance of flow was reduced at the bird-beak location due to boundary conditions and change of geometry after TEVAR. Stent-graft protrusion with partial coverage of the origin of the left subclavian artery produced a disturbance of flow in this vessel. Strong velocity increase and flow disturbance were found at the aortic narrowing in the descending thoracic aorta when comparing B and C, while no effect was seen on aortic arch hemodynamics.

Conclusion: CFD may help physicians to understand aortic hemodynamic changes after TEVAR, including the change in aortic arch geometry, the effects of a bird-beak configuration, the supra-aortic flow distribution, and the aortic true lumen dynamics. This study is the first step in establishing a computational framework that, when completed with patient-specific data, will allow us to study thoracic aortic pathologies and their endovascular management.

J Endovasc Ther. 2014;21:791–802

This work was partially funded by Cariplo Foundation (project no. 2009.2822) and Regione Lombardia and CINECA Consortium through a LISA (Laboratory for Interdisciplinary Advanced Simulation) Initiative 2013 grant for computational facilities.

The authors declare no association with any individual, company, or organization having a vested interest in the subject matter/products mentioned in this article.

Corresponding author: Santi Trimarchi, MD, PhD, Thoracic Aortic Research Center, Director, Policlinico San Donato IRCCS, University of Milan, Piazza Malan 2, 20097 San Donato Milanese, Italy. E-mail: *santi.trimarchi@unimi.it*; *satrimarchi@gmail.com*; *santi.trimarchi@grupposandonato.it*

 doi:10.1583/14-4778MR.1 ***Available at www.jevt.org***

Key words: computational fluid dynamics, biomechanics, aorta, thoracic endovascular aortic repair, bird-beak, stent-graft, flow disturbance, true lumen narrowing

Thoracic endovascular aortic repair (TEVAR) has been established as an important treatment modality for thoracic aortic pathologies, such as type B aortic dissection and thoracic aortic aneurysm.[1–3] TEVAR has been proven to be safe and effective, with satisfactory midterm outcome.[4–7] Recently, more positive long-term outcomes have been reported for acute and subacute dissections treated with TEVAR.[8,9]

Nevertheless, TEVAR has been associated with device-related complications, including endoleak, stent-graft migration or collapse, and retrograde type A dissection.[7,10,11] Since the outcome of TEVAR relies on the biomechanical properties of the aortic wall and of the stent-graft, anatomical complexity is not surprisingly the most important reason for early and late stent-graft failure. Among the several anatomical factors that may impact the results of TEVAR, the length and curvature of the proximal landing zone, along with its specific aortic wall characteristics, may be the most influential.

See commentary page 803

In particular, endovascular treatment of aortic arch disease frequently necessitates a proximal landing zone located at the inner curvature of the aortic arch, which is likely to be a significant risk factor for endoleak and stent-graft collapse.[12] Due to the stiffness of the stent-graft, increased angulation may decrease the length of the graft in contact with the aortic wall. Specifically, apposition of the device to the aortic wall at the inner curvature of the aortic arch can result in a so-called bird-beak configuration, which refers to the wedge-shaped gap between the undersurface of the stent-graft and the aortic wall seen on imaging (Fig. 1).[12]

The current literature discussing the incidence of bird-beak configurations and their impact on patient outcome is heterogeneous; most reports are case series[13] or retrospective studies.[10,14,15] A significant correlation between the presence of a bird-beak configuration and the risk of endoleak (type Ia) at the proximal landing zone has been reported.[12,16] Furthermore, the longer the bird-beak length, the greater the risk for endoleak formation.[12] On the other hand, the bird-beak configuration is thought to have a benign effect in most patients, except for younger patients with higher cardiac output.[10]

Another important aspect in these patients is that many require coverage of the left subclavian artery (LSA) to achieve adequate sealing during TEVAR. LSA coverage can cause significant changes in the supra-aortic branch hemodynamics, and patients with LSA coverage showed increased prevalence of neurological complications and endoleaks.[17,18]

All these concerns may be addressed by quantitative analysis of postoperative aortic hemodynamics and its correlation with adverse outcomes. In the present study, a clinical case with bird-beak configuration (Fig. 1) after TEVAR was investigated using computational fluid dynamics (CFD) analyses based on the patient-specific geometry reconstructed from imaging datasets. The results are compared to similar cases reported in the literature.

METHODS

Patient Data

Pre- and postoperative computed tomographic angiography (CTA) data from a patient treated with TEVAR were used to evaluate the anatomical changes induced by the stent-graft and to generate the computational network essential for CFD analysis. The patient was an asymptomatic 51-year-old man with a 6.1-cm thoracic aortic aneurysm (Fig. 2A) discovered 5 years after uncomplicated type B aortic dissection (medically treated). The false lumen was partially perfused (Fig. 2B). He received two C-TAG stent-grafts (W.L. Gore & Associates. Inc., Flagstaff, AZ, USA) after revascularization of the LSA,

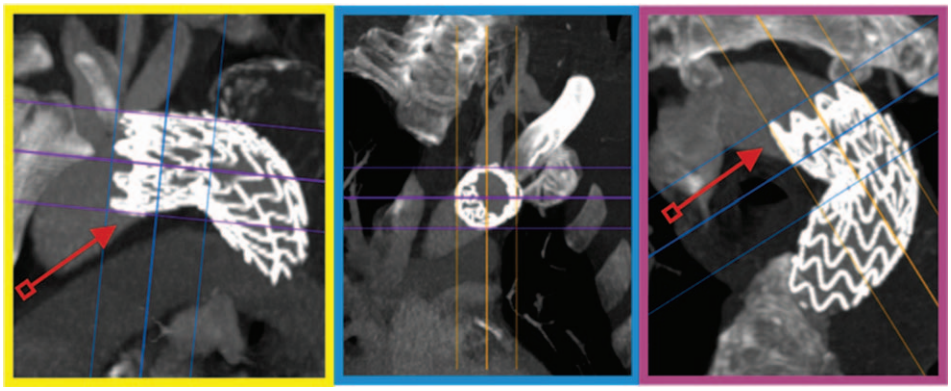

Figure 1 ◆ Thin-slab maximum intensity projection shows a bird-beak configuration (arrowhead). At the proximal end, the stent-graft was imperfectly apposed to the lesser inner curvature of the aortic arch, resulting in a wedge-shaped gap between the undersurface of the stent-graft and the aortic wall. A color version is available online at *www.jevt.org*.

whose origin was in proximity to the proximal landing zone. Under general anesthesia, the C-TAG devices (34×34×200 mm and 28×28×150 mm) were deployed partially covering the origin of the LSA. Rapid ventricular pacing (200 beats/min) for 50 seconds was used during deployment; no post-deployment balloon molding was performed. Successful exclusion of the aneurysm was observed using intraoperative angiography and transesophageal echography. No postoperative complications were reported. The postoperative CTA (Fig. 1) at 3 days showed a bird-beak configuration of the stent-graft. At 6 months and 1 year, imaging showed successful exclusion of the aneurysm without endoleak.

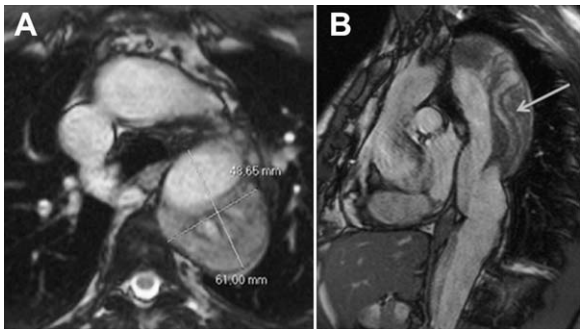

Figure 2 ◆ Preoperative medical images of the (**A**) post-dissecting aneurysm 5 years after uncomplicated type B aortic dissection, with a maximum diameter of 6.1 cm at the level of the left hemi-arch. (**B**) Partial perfusion in the false lumen (arrow) with post-dissecting aneurysm formation.

Image Processing

Comparison between pre- and postoperative stent-graft/vessel configuration relies on a precise assessment and reconstruction of the 3-dimensional (3D) profile of the vessel lumen, thrombus, and calcifications (Fig. 3). The engineering details of the image processing pathway are outlined in Appendix A.

Looking at Figure 3, the proximal graft protruded into the lumen at the inner curvature of the aortic arch (i.e., bird-beak configuration) and only partially (61%) covered the origin of the LSA (Fig. 3). Following the definitions proposed by Pasta et al.,[19] two main variables of the graft geometry were measured: the protrusion extension, defined as the length of graft not in contact with the aortic wall, and the angle between the inner curvature of the aorta and the protruded segment of the graft wall. For the case under investigation, protrusion extension was 1.55 cm and the angle 51°.

Further, the stent-graft significantly narrowed the lumen diameter in the upper part of the arch, immediately distal to the LSA. At the level of the lower descending thoracic aorta, the distal stent-graft was unable to completely resolve the narrowing of the true lumen induced by the pressurization of the false lumen that was present preoperatively. With the lumen area of the upper descending thoracic aorta as a reference, the stenosis is 87% preoperatively, while after TEVAR it is 65%, which implies that the intervention

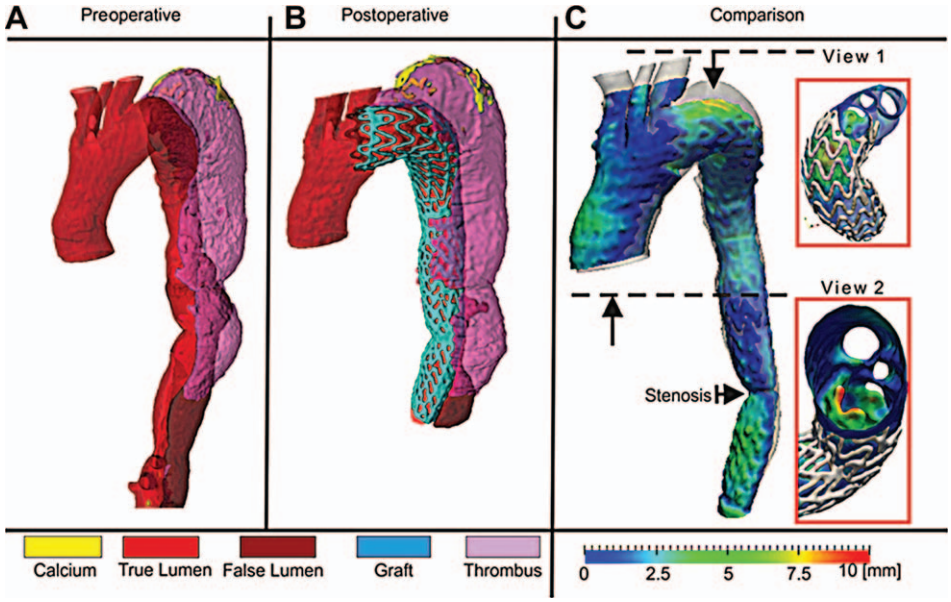

Figure 3 ◆ A 3D reconstruction of the preoperative (**A**) and postoperative (**B**) aorta. (**C**) Comparison of the two configurations depicts the contour plot of the point-wise distances between the pre- and postoperative lumens. A color version is available online at *www.jevt.org*.

contributed to true lumen expansion, but the stenosis remained significant (i.e., ≥50%).

CFD Cases

Hemodynamics were assessed in both the global aorta and in 3 specific aortic regions: (1) the inner curvature of the aortic arch where the bird-beak was present, (2) the partially covered origin of the LSA, and (3) the distal part of the descending thoracic aorta characterized by the narrowed true lumen. Besides using the true pre- and postoperative scenario, computer-based simulations were also adopted to explore potential scenarios. As a result, this study was based on 3 different CFD analyses with specific aortic lumen configurations: Case A was the preoperative lumen, Case B was the postoperative lumen, and Case C was the postoperative lumen computed without stenosis of the distal descending aorta. Case C was obtained fictitiously, resolving the distal stenosis in order to create a smooth, more physiological profile of the descending aorta. This scenario was conducted to investigate a virtual setting wherein the stenosis would be mitigated or resolved during endovascular treatment. When cases A and B were compared, the focus was on the flow in the aortic arch and the bird-beak effect. Therefore, in case A, the distal descending aortic tract, featuring the false lumen and presence of one or more (re-)entry tears, was not included. In contrast, when comparing cases B and C, the analysis included the impact of the distal stenosis in the descending thoracic aorta, and therefore the distal descending aorta was incorporated in this evaluation.

During the analysis of the numerical results, attention was focused on certain time points in the cardiac cycle and specific regions of the aorta. Three time moments were selected, expressed as fractions of the cardiac cycle: T1 was the point of maximum acceleration of blood flow, T2 corresponded to the systolic peak, and T3 was the point of maximum deceleration of blood flow. Specific regions of the aorta were evaluated with the focus on the 3 cases described in the previous section, i.e., the inner curvature of the aortic arch for cases A and B, the origin of the LSA for cases A and B, and the distal part of the thoracic descending aorta for cases B and C.

The aortic hemodynamics of the clinical case under investigation were reconstructed through CFD analysis, which is a computer-

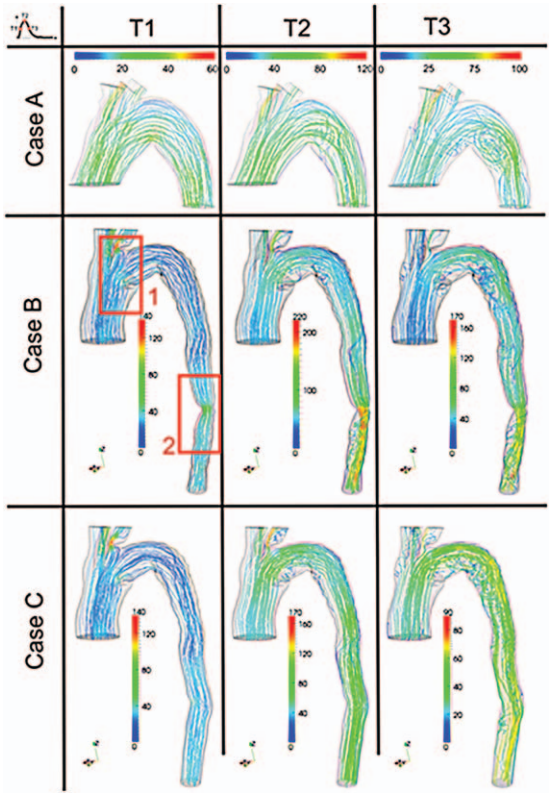

Figure 4 ◆ Velocity streamlines for each investigated case (A–C) for 3 different time points (T1–T3). The corresponding velocity magnitude (cm/s) is used to color each streamline. A color version is available online at *www.jevt.org*.

based simulation able to solve in an approximate manner the Navier-Stokes equations for incompressible fluid dynamics. For the problem under investigation, this was considered a valid model. The computational domain (mesh) of our study resembled the volume occupied by the arterial blood, with the stent-graft included in the simulation as part of the computational domain boundaries. Therefore, the stent-graft appeared as a sort of footprint in the aortic lumen as shown in Figure 3. Because aortic hemodynamics was our primary focus of the analysis, the wall of the computational domain (i.e., the luminal surface of the aorta) partially covered with stent-graft(s) was considered to be rigid. Consequently, both device and vessel displacement during the cardiac cycle due to pulsatile loading was neglected. Furthermore, we adopted a no-slip boundary condition, i.e., the blood velocity at the wall was considered null. This boundary condition was used for modeling viscous fluids on nonporous walls; subsequently, this approach assumed impermeability of the stent-graft Dacron cover. The pathways for generating the computational domain (the mesh), numerical model, and simulation processing are described in Appendix B.

RESULTS

Velocity Streamlines

Numerical simulations provided the velocity (vector quantity) and the pressure in the nodes of the grid at 3 different time points. Other variable functions of velocity and pressure were computed as the streamlines, which represent the direction of the blood flow at a given time point.[20] A global view of the streamlines of blood velocity at the selected time instants for each of the investigated cases is demonstrated in Figure 4.

Case A vs. B: Preoperative vs. Postoperative Scenario

The postoperative aortic lumen showed 3 sharp changes of the geometry, one at the bird-beak location, one at the distal aortic arch, and one at the distal descending thoracic aorta; the sharpness of the geometrical changes led to boundary layer separation, ultimately resulting in blood flow disturbance, contoured by a red box in Figure 4. Similarly, stent-graft protrusion into the lumen at the level of the aortic arch resulted in significant coverage of the LSA origin, which produced the backward-facing step geometry of the lumen profile. This disturbed the flow, which was clearly not present in the other supra-aortic branches (i.e., the brachiocephalic trunk and the left common carotid artery).

Case B vs. C: Postoperative vs. Postoperative Without Stenosis

The stenosis of the distal thoracic aorta due to the compression of the true lumen by the false lumen caused a strong velocity increase and flow disturbance (Fig. 4). However, these effects did not introduce significant changes

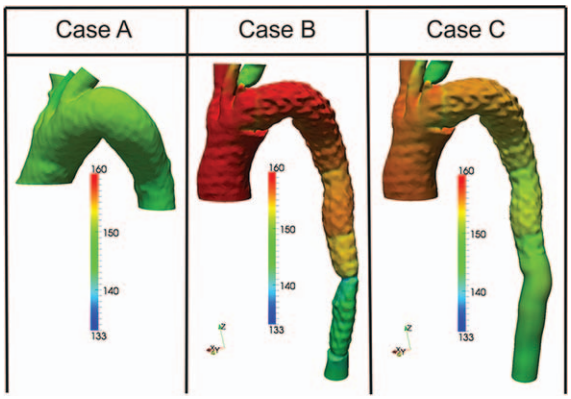

Figure 5 ◆ Contour plots representing the distribution of blood pressure (mmHg) along the aorta in the 3 cases at the systolic peak. A color version is available online at *www.jevt.org*.

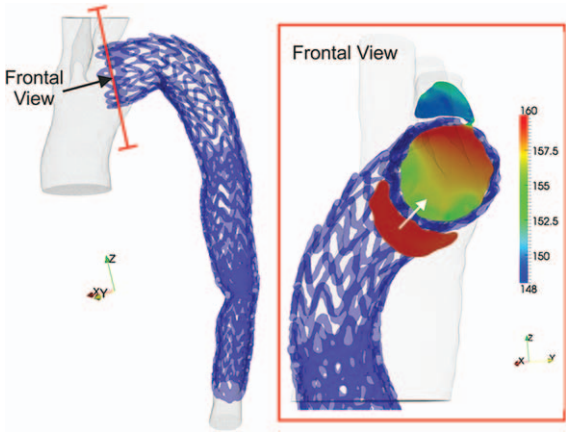

Figure 6 ◆ Contour plot of the pressure (in mmHg) distribution along a cross-section in the bird-beak region for case B. A color version is available online at *www.jevt.org*.

in the flow distribution at the systemic level. The pattern of streamlines in case C suggested that the stenosis of the distal descending thoracic aorta had no effect on arch hemodynamics. At the same time, the recovery of a smooth, physiological lumen profile eliminated the flow disturbance in this region, highlighted by the results of cases B and C (Fig. 4).

Pressure

The pressure distribution along the aorta at the systolic peak for the 3 investigated cases is shown in Figure 5. For both postoperative configurations (case B and C), a pressure drop (i.e., almost 10 mmHg) induced by the stent-graft was observed, notable at the partially covered origin of the LSA. The bird-beak effect and the stenosis resulted in a significant reduction in lumen patency and therefore in an increased pressure drop due to the Venturi effect (Bernoulli's principle). On the other hand, the pressure field was smooth in the brachiocephalic trunk, in the left common carotid artery, and in the aortic arch, similar to the preoperative case. It is worth noting that in case B the stenosis induced a higher overall pressure compared to the case without stenosis (case C). The global variation of pressure is ~5 mmHg. This comparison shows clearly that removal of the lumen narrowing mitigated significantly the local pressure drop (i.e., around 15 mmHg), which is visible in case C. Additionally, Figure 6 demonstrates a virtual cross-sectional view of the aortic arch at the level of the bird-beak, revealing a transmural pressure load difference of almost 10 mmHg between the undersurface and the luminal surface of the stent-graft.

DISCUSSION

The present study addressed the quantitative analysis of aortic hemodynamics after TEVAR. Although the main clinical concern was directed to the impact of a bird-beak configuration, the CFD simulations demonstrated, as a translational finding, that the local hemodynamic condition is impaired and blood flow is disturbed in two other important areas: (1) the origin of the LSA that was only partially covered by the stent-graft and (2) the stenosis of the distal descending thoracic aorta.

The computed preoperative hemodynamics of this case compared to the postoperative condition showed that flow velocity in the entire thoracic aorta was decreased after TEVAR. In addition, the presence of the bird-beaked stent-graft was not associated with relevant increased disturbance of flow in the aortic arch. These findings might be particularly attributed to the boundary conditions and also to the distinctive features of the preoperative geometry. These results can

therefore not be generalized, and it might be expected that the presence of a bird-beak configuration actually should increase the disturbance of flow. However, arch angulation after TEVAR might potentially be reduced, and this could mitigate the impact of the bird-beak configuration on aortic arch blood flow disturbance. In contrast, first-generation stent-grafts have been associated with stent-graft–related complications such as stent-graft collapse.[14] However, with the introduction of Gore's second-generation conformable TAG device with its improved flexibility and uncovered proximal end to reduce interference with the bloodstream, no major stent-graft–related complications, including infolding, have been recorded.[21]

Figure 6 demonstrated the contour plot of the pressure in the bird-beak section, which clearly revealed a transmural pressure load difference (almost 10 mmHg) between the undersurface and the luminal surface of the graft. This pressure drop, which is congruent with the result reported by Pasta et al.,[19] demonstrates that the part of the stent-graft protruding into the lumen is exposed to hemodynamic forces, which solely indicate a potential risk of graft infolding or collapse. Despite this pressure load difference, no stent-graft–related complications were present in this patient, and further structural analyses could assess the importance of this finding.

As expected, the removal of the distal true lumen stenosis reduced significantly both the flow disturbance and the pressure drop across the involved arterial tract. Beside the clinical relevance of these specific findings, the value of these simulations is clear: CFD analyses depict important flow effects that result from the specificities of patient vessel geometry. These results may reinforce the potential impact of the translation of knowledge from computational biomechanics to clinical practice and vice versa. It is important to note that this process is steadily evolving; in fact, this analysis follows the path described by other numerical studies regarding post-TEVAR hemodynamics. Lam et al.[22] in 2008 computed through CFD the displacement force acting on a stent-graft; using the information obtained from CT imaging, they tailored an ideal model of both the aorta and the implanted stent-graft to patient-specific geometrical features in order to investigate the impact of stent-graft apposition on the displacement force acting on the device. The same approach has been pursued also in other studies.[23,24]

In 2009, Figueroa et al.[25] assessed the displacement forces acting on thoracic stent-grafts using CFD, proving that computational methods can enhance the understanding of the magnitude and orientation of the loads experienced in vivo by thoracic stent-grafts and therefore improve their design and performance. In 2011, Prasad and colleagues[26,27] evaluated through computer-based simulations the biomechanical and hemodynamic forces acting on the intermodular junctions of a multicomponent thoracic stent-graft, focusing on the development of type III endoleak. Moving from medical image analysis and using CFD combined with computational solid mechanics techniques, they predicted critical zones of intermodular stress concentration and frictional instability, which effectively matched the location of the type III endoleak observed during follow-up CT imaging after 4 years.

In 2012, Midulla et al.[28] used magnetic resonance (MR) angiography followed by cardiac-gated cineangiography sequences covering the whole thoracic aorta to obtain CFD boundary conditions and track aortic wall movements. They evaluated 20 patients characterized by different aortic lesions, showing the feasibility and potential of dedicated CFD analysis to provide detailed functional analysis of the thoracic aorta after stent-graft implantation. More recently, Pasta et al.[19] described a computational study aimed at assessing the biomechanical implications of excessive postoperative graft protrusion into the aortic arch by simulating the structural load and quantifying the fluid dynamics on the graft wall protrusion. Their findings suggested that protrusion extension conveys an apparent risk of distal end-organ malperfusion and proximal hypertension, being also proportional to a pressure load acting across the graft wall, potentially inducing stent-graft collapse. These results were also confirmed by the findings in this study.

In our study, the CFD analyses detected the presence of significant hemodynamic turbulence in the distal descending aorta. Although this observation was not associated with changes in thoracic aortic hemodynamics, it was considered an important translational finding and might be of importance when considering TEVAR for chronic type B dissection.

Limitations

The investigation of a single clinical case is a major limitation of the present study because it does not allow generalization of the study conclusion. However, it is worth noting that the data necessary to perform the presented analyses require extensive integration of interdisciplinary knowledge. Indeed, this consideration calls for a deeper and conscious collaboration between clinicians and biomedical engineers/researchers. In that regard, the present study poses the basis for further studies involving a larger clinical dataset.

The lack of patient specificity for the inflow and outflow boundary conditions is an important limitation of this study. To overcome this problem, a prospective study with prior patient consent to measure flows outside of the standard of care for the (endovascular) management of thoracic aortic disease is warranted. Specifically, the validation of the proposed results and the use of patient-specific boundary conditions should be investigated. For both purposes, flow rates derived from MR images will be used in future studies of our group and other multidisciplinary study teams. Nevertheless, the present study shows the translational potential of a multidisciplinary approach to analyze TEVAR; for this reason, we believe that the case under investigation may be of interest despite the absence of an endoleak or other postoperative complications.

Future investigations could enhance the clinical impact of CFD by identifying a case with confirmed endoleak and asking the subject to consent to a phase-contrast MR imaging study to measure the flow velocities in the supra-aortic branches and descending aorta. This will lead to simulations with patient-specific outflow boundary conditions, at least postoperatively. The same approach can be used prior to intervention in order to compare pre- and post-TEVAR hemodynamics. Although we have not adopted patient-specific blood flow measurements, the reason why the present results are reliable is twofold: (1) we have used state-of-the-art outflows accounting for peripheral circulation and (2) the prediction of flow disturbance at the level of the distal thoracic descending aorta, highlighted by the simulations, has not been addressed by a pure clinical approach. The CFD analyses performed in this study for both pre- and postoperative situations form the base for future studies with implementation of the patient-specific boundary conditions.

Conclusion

Computational fluid dynamics gives important information about aortic hemodynamics after TEVAR. In particular, it may help physicians to understand the change of aortic arch geometry, the effects of the bird-beak configuration, the supra-aortic flow distribution, and aortic true lumen stenosis. This study is the first step in establishing a computational framework that, when completed with patient-specific data, will allow us to study thoracic aortic pathologies and endovascular management.

Acknowledgments: The authors would like to acknowledge Matteo Pegorer, MD, and Sara Segreti, MD, for collecting medical images; Eng. Stefania Marconi and Dr. Marina Piccinnelli for the medical image elaboration, and Tiziano Passerini, PhD, for his support regarding the computational analysis. Ferdinando Auricchio and Michele Conti acknowledge the support of the Ministero dell'Istruzione, dell'Università e della Ricerca (project no. 2010BFXRHS) and an ERC Starting Grant through ISOBIO (Isogeometric Methods for Biomechanics; project no. 259229).

APPENDICES

Appendix A

The 3D reconstructions of the two CTA datasets began with segmentation using the open-source software ITK-Snap 16 according to the approach proposed by Auricchio et al.[29] The resulting 3D models included thrombus, cal-

cifications, and stent-grafts. A preliminary analysis was performed to evaluate the change induced by graft apposition. First, the postoperative lumen profile was registered onto the preoperative one using the VMTK module *vmtkicpregistration*, available within the vascular modeling toolkit (*www.vmtk.org*). Second, the point-wise distance between the two surfaces was measured using the VMTK module *vmtksurfacedistance*. The results of this preliminary analysis are depicted in Figure 3. The two main quantities pertaining to graft protrusion geometry (protrusion extension and the angle between the inner curvature of the aorta and the protruded segment of the graft wall) were measured using tools available in Osirix (*www.osirix-viewer.com*), exploiting the 2D multiplanar reconstructions to select the cutting plane corresponding to the maximum graft protrusion.

Appendix B

Numerical simulations solving the Navier-Stokes (NS) equations for incompressible fluids in an unsteady state in the region of interest (Ω) were carried out. Newtonian rheology was assumed (i.e., constant viscosity), which is commonly considered correct for large and medium size vessels.[30] The values u (x; y; z; t) and p (x; y; z; t) were blood velocity and pressure, respectively; ρ denoted the constant blood density and ν represented the viscosity. The NS equation reads:

$$\rho\frac{\partial \boldsymbol{u}}{\partial t} + \rho(\boldsymbol{u}\cdot\nabla)\boldsymbol{u} - \nabla\cdot\left(\nu(\nabla\boldsymbol{u} + \nabla^T\boldsymbol{u})\right) + \nabla\boldsymbol{p} = 0$$

$$\nabla\cdot\boldsymbol{u} = 0,$$

for x; y; z ε Ω and $0 < t \leq T$, where T is the duration of a time interval of interest. These equations were completed for the initial and the boundary conditions. The initial conditions were null velocity and pressure fields, corresponding to a fluid at rest. Three types of boundaries were distinguished. Since particular patient-specific data were not available for this case, data from physical considerations (for the wall and stent struts) or from the literature (for the inflow/outflow sections) were retrieved as discussed below.

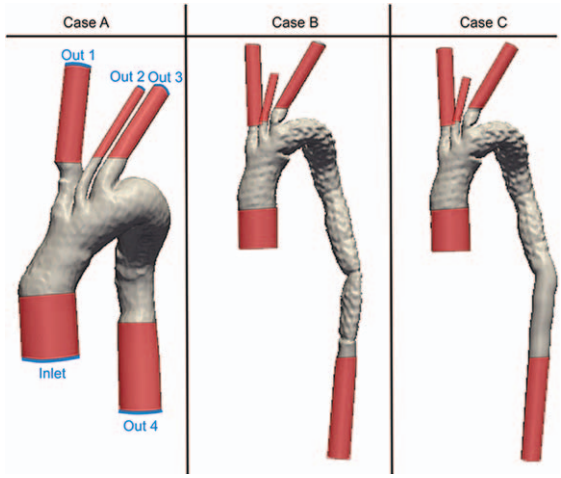

Figure A1 ◆ Computational domains for the 3 investigated cases. The flow extensions are highlighted in light red, while the reference sections for both the inlet and outlet conditions are highlighted in blue. Inlet refers to the inlet section of the ascending aorta, Out 1 is the outlet section of the brachiocephalic trunk, Out 2 is the left common carotid artery, Out 3 is the left subclavian artery, and Out 4 is the descending thoracic aorta. A color version is available online at *www.jevt.org*.

On the arterial wall and stent struts in the lumen, null velocity was prescribed, which corresponded with a rigid stented artery. A more accurate model would include the interaction of fluid and structure, but the computational costs would be significantly higher, and the accuracy advantage is questionable, since the structural model for the arterial wall (different from the blood model given by the NS equations) is affected by several uncertainties.

On the inflow section (Fig. A1) slightly distal to the aortic valve, a flow rate was prescribed by selecting a velocity profile yielding at each instant the flow waveform considered in the literature.[31]

On the outflow sections (Fig. A1), we prescribed conditions based on a classical 3-element Windkessel modeling of the distal circulation. The peripheral impedance at each outflow section was represented by two resistances, R_1 and R_2, and a compliance C (RCR model). The specific values of those parameters were taken from Kim et al.[32] The region of interest was artificially extended by

inserting regular cylindrical regions at the distal sections, called flow extensions. The role of these regions was to reduce the impact of modeling choices and uncertainties in the boundary conditions on the numerical results in the region of interest. Flow extensions have been added with the open source library vascular modeling toolkit (*www.vmtk.org*) as highlighted in Figure A1. The same values of R_1, R_2, and C were adopted for all the cases; this assumption can be justified also for case A, where the distal part of the thoracic aorta was not included in the computational grid, under the hypothesis that the excluded vascular tract had a low hydraulic resistance when compared with the imposed RCR boundary condition.

Numerical simulation was based on the finite element method. In each of the 3 cases, the artery $\Omega_{a,b,c}$, reconstructed from the images and modified with the flow extensions, was first divided into subregions called elements, followed by computation of polynomial solution. Tetrahedral elements were used, which are particularly versatile and suited for complex geometries such as the ones considered here. Meshing was carried out using the methods available in the VMTK library; the details of the mesh for each of the investigated cases are reported in the Table. No particular attention was given to generate the so-called boundary layer mesh because in all the cases the mesh size was small enough to also catch the flow patterns close to the border; furthermore, the main interest was not on wall shear stress computation.

The problem was solved over 5 heartbeats, arguing that the solution computed in the last heartbeat reliably approximated periodic pulsatile conditions. To perform the simulations, the open C++ library LifeV (*www.lifev.org*) was used, which was developed by some of the co-authors in a collaborative project including EPF (Lausanne, Switzerland), Politecnico di Milano (Milan, Italy), INRIA (Paris, France), and Emory University (Atlanta, GA, USA). As a tradeoff between accuracy and computational costs, the so-called P1 bubble elements were used (a special piecewise cubic approximation) for the velocity and P1 elements (piecewise linear) for the pressure. Simulations were carried out on a Dell R815 computer (4 AMD Opteron 6272 CPUs with 16 cores/CPU, 1 thread/core, 252 GB of RAM, and data storage of 260 GB) hosted by the University of Pavia (*www.unipv.it/compmech/nume-lab.html*).

As clearly shown by the number of degrees of freedom of each performed simulation (Table), the amount of data generated was relevant and required a dedicated post-processing analysis. We performed such an analysis using Paraview, an open-source, general-purpose, scientific visualization software available at *www.paraview.org*.

TABLE
Mesh Details for Cases A, B, and C

Case	Nodes	Elements	Degrees of Freedom
A	258,115	1,545,810	5,669,890
B	1,219,858	6,659,921	24,859,195
C	883,994	5,375,521	19,662,539

A: preoperative, B: postoperative, and C: postoperative without distal stenosis.

REFERENCES

1. Dake MD, Kato N, Mitchell RS, et al. Endovascular stent-graft placement for the treatment of acute aortic dissection. *N Engl J Med*. 1999;340:1546–1552.
2. Dake MD, Miller DC, Semba CP, et al. Transluminal placement of endovascular stent-grafts for the treatment of descending thoracic aortic aneurysms. *N Engl J Med*. 1994;331:1729–1734.
3. Nienaber CA, Fattori R, Lund G, et al. Nonsurgical reconstruction of thoracic aortic dissection by stent-graft placement. *N Engl J Med*. 1999;340:1539–1545.
4. Cheng D, Martin J, Shennib H, et al. Endovascular aortic repair versus open surgical repair for descending thoracic aortic disease a systematic review and meta-analysis of comparative studies. *J Am Coll Cardiol*. 2010;55:986–1001.
5. Czerny M, Funovics M, Sodeck G, et al. Long-term results of thoracic endovascular aortic repair in atherosclerotic aneurysms involving the descending aorta. *J Thorac Cardiovasc Surg*. 2010;140(6 Suppl):S179–184.

6. Demers P, Miller DC, Mitchell RS, et al. Midterm results of endovascular repair of descending thoracic aortic aneurysm with first-generation stent-grafts. *J Thorac Cardiovasc Surg*. 2004; 127:664–673.
7. Eggebrecht H, Herold U, Kuhnt O, et al. Endovascular stent-graft treatment of aortic dissection: determinants of post-interventional outcome. *Eur Heart J*. 2005;26:489–497.
8. Fattori R, Montgomery D, Lovato L, et al. Survival after endovascular therapy in patients with type B aortic dissection: a report from the International Registry of Acute Aortic Dissection (IRAD). *JACC Cardiovasc Interv*. 2013;6: 876–882.
9. Nienaber CA, Kische S, Rousseau H, et al. Endovascular repair of type B aortic dissection: long-term results of the randomized investigation of stent-grafts in aortic dissection trial. *Circ Cardiovasc Interv*. 2013;6:407–416.
10. Kasirajan K, Dake MD, Lumsden A, et al. Incidence and outcomes after infolding or collapse of thoracic stent-grafts. *J Vasc Surg*. 2012;55:652–658.
11. Tolenaar JL, van Bogerijen GH, Eagle KA, et al. Update in the management of aortic dissection. *Curr Treat Options Cardiovasc Med*. 2013;15: 200–213.
12. Ueda T, Fleischmann D, Dake MD, et al. Incomplete endograft apposition to the aortic arch: bird-beak configuration increases risk of endoleak formation after thoracic endovascular aortic repair. *Radiology*. 2010;255:645–652.
13. Shukla AJ, Jeyabalan G, Cho JS. Late collapse of a thoracic endoprosthesis. *J Vasc Surg*. 2011;53:798–801.
14. Canaud L, Alric P, Desgranges P, et al. Factors favoring stent-graft collapse after thoracic endovascular aortic repair. *J Thorac Cardiovasc Surg*. 2010;139:1153–1157.
15. Jonker FH, Schlösser FJ, Geirsson A, et al. Endograft collapse after thoracic endovascular aortic repair. *J Endovasc Ther*. 2010;17:725–734.
16. Piffaretti G, Mariscalco G, Lomazzi C, et al. Predictive factors for endoleaks after thoracic aortic aneurysm endograft repair. *J Thorac Cardiovasc Surg*. 2009;138:880–885.
17. Matsumura JS, Lee WA, Mitchell RS, et al. The Society for Vascular Surgery Practice Guidelines: management of the left subclavian artery with thoracic endovascular aortic repair. *J Vasc Surg*. 2009;50:1155–1158.
18. Sze DY, van den Bosch MA, Dake MD, et al. Factors portending endoleak formation after thoracic aortic stent-graft repair of complicated aortic dissection. *Circ Cardiovasc Interv*. 2009; 2:105–112.
19. Pasta S, Cho JS, Dur O, et al. Computer modeling for the prediction of thoracic aortic stent-graft collapse. *J Vasc Surg*. 2013;57:1353–1361.
20. Erhard P, Etling D, Muller U, et al. *Prandtl-Essentials of Fluid Mechanics*, 3 ed. Springer: Berlin Heidelberg; 2010.
21. Farber MA, Giglia JS, Starnes BW, et al. Evaluation of the redesigned conformable GORE TAG thoracic endoprosthesis for traumatic aortic transection. *J Vasc Surg*. 2013;58: 651–658.
22. Lam SK, Fung GS, Cheng SW, et al. A computational study on the biomechanical factors related to stent-graft models in the thoracic aorta. *Med Biol Eng Comput*. 2008;46: 1129–1138.
23. Cheng SW, Lam ES, Fung GS, et al. A computational fluid dynamic study of stent-graft remodeling after endovascular repair of thoracic aortic dissections. *J Vasc Surg*. 2008; 48:303–310.
24. Fung GS, Lam SK, Cheng SW, et al. On stent-graft models in thoracic aortic endovascular repair: a computational investigation of the hemodynamic factors. *Comput Biol Med*. 2008; 38:484–489.
25. Figueroa CA, Taylor CA, Chiou AJ, et al. Magnitude and direction of pulsatile displacement forces acting on thoracic aortic endografts. *J Endovasc Ther*. 2009;16:350–358.
26. Figueroa CA, Zarins CK. Computational analysis of displacement forces acting on endografts used to treat aortic aneurysms. In: McCloughlin T, ed. *Studies in Mechanobiology, Tissue Engineering and Biomaterials*. Vol 7. Springer: Berlin Heidelberg; 2011:221–246.
27. Prasad A, To LK, Gorrepati ML, et al. Computational analysis of stresses acting on intermodular junctions in thoracic aortic endografts. *J Endovasc Ther*. 2011;18:559–568.
28. Midulla M, Moreno R, Baali A, et al. Haemodynamic imaging of thoracic stent-grafts by computational fluid dynamics (CFD): presentation of a patient-specific method combining magnetic resonance imaging and numerical simulations. *Eur Radiol*. 2012;22:2094–2102.
29. Auricchio F, Conti M, Marconi S, et al. Patient-specific aortic endografting simulation: from

diagnosis to prediction. *Comput Biol Med*. 2013;43:386–394.
30. Formaggia L, Quarteroni A, Veneziani A. *Cardiovascular Mathematics*. Springer: Berlin; 2009.
31. Morbiducci U, Ponzini R, Rizzo G, et al. In vivo quantification of helical blood flow in human aorta by time-resolved three-dimensional cine phase contrast magnetic resonance imaging. *Ann Biomed Eng*. 2009;37:516–531.
32. Kim HJ, Vignon-Clementel IE, Figueroa CA, et al. On coupling a lumped parameter heart model and a three-dimensional finite element aorta model. *Ann Biomed Eng*. 2009;37:2153–2169.